Original research article

Institution of MECHANICAL ENGINEERS
Journal of SYSTEMS AND CONTROL ENGINEERING

Proc IMechE Part I:
J Systems and Control Engineering
1–19

DOI: 10.1177/09596518261435670
journals.sagepub.com/home/pii
Sage

Modeling and characteristic analysis of the multilayer bimorph and deflector-feedback rod assembly in a deflector jet servo valve

Yunqi Li[1], Shiyong Niu[2], Yuchuan Zhu[1], Jie Ling[1] and Jiahao Kang[2]

Abstract

The deflector jet servo valve driven by multilayer bimorph achieves exceptional performance for advanced aerospace applications, with critical advantages of fast response, high precision and compact structure. The valve output characteristics is fundamentally determined by the output characteristics of its multilayer bimorph and deflector-feedback rod assembly, where existing models fail to accurately predict behavior under limited working conditions. This study develops a mathematical model to precisely characterize the output characteristics of assembly, incorporating adjustable clamping length and reduction of effective driving force. With finite element analysis and experiments, static characteristics of the assembly are analyzed. Experimental validation demonstrates the accuracy of model, reducing maximum relative errors by 50.5% in assembly end feedback force prediction and 66% in deflector displacement estimation compared to conventional approaches. This work provides not only essential theoretical support for multilayer bimorph applications in complex structural load, but also provides theoretical support for developing precise control algorithms with mechanical feedback. The improved model enables optimization of servo valve design and assembly precision while maintaining system performance.

Keywords

piezoelectric actuator, multilayer bimorph, mathematical model, static characteristics, servo valve

Received: 15 August 2025; accepted: 24 February 2026

Introduction

Electro-hydraulic servo valves, as core components of electro-hydraulic servo control systems, are widely used in aerospace with the advantages of high precision, small size, fast response.[1,2] Conventional two-stage servo valves employ torque or force motors coupled with hydraulic amplifiers (as first stage) to drive sliding spools (as second stage).[3,4] However, torque or force motors have present following limitations: structural complexity; challenging installation and adjustment requirements; difficulties in enhancing bandwidth.

To address these limitations, piezoelectric actuators offer simplified structure, reduced weight, faster response, magnetic interference immunity, and higher reliability.[5–8] These advantages make electro-hydraulic servo valves driven by piezoelectric actuators ideal for aerospace applications where exist strict mass and size limitations.[9,10] Design and installation of piezoelectric actuators are especially critical as they directly determine output precision and output characteristics of these servo valves.

There are three main types of piezoelectric actuators used to drive electro-hydraulic servo valves[11,12]: axial actuator (stack),[13,14] ring bender[15,16] and rectangular bender.[17] While axial stacks intrinsically provide high output force, their practical implementation requires displacement amplification mechanisms that inevitably compromise dynamic response.[18] In contrast, ring and rectangular benders provide greater output displacements

[1]College of Mechanical and Electrical Engineering, Nanjing University of Aeronautics and Astronautics, China
[2]AVIC Xi'an Flight Automatic Control Research Institute, China

Corresponding author:
Yuchuan Zhu, College of Mechanical and Electrical Engineering, Nanjing University of Aeronautics and Astronautics, No. 29, Yudao Street, Qinhuai District, Nanjing 210016, P. R. China.
Email: meeyczhu@nuaa.edu.cn

at lower voltages, though with reduced output forces.[19] When the length of rectangular benders equals the outer diameter of ring benders, the rectangular benders can provide greater output displacements.[20] This study employs a multilayer bimorph (a type of rectangular benders), as it optimally meets servo valve requirements for displacement, force and compactness.

While multilayer bimorphs are widely used in pneumatic valves and sensors with simple load conditions,[21,22] application in hydraulic servo valves introduces significant challenges due to two key factors: operation in oil that introduce fluid-structure interactions; precisely driving the flexible loads with complex structure.

To address oil-immersion operational challenges, scholars have studied the mathematical model of a single multilayer bimorph. Based on electromechanical behavior of free bimorph analyzed by Jan,[23] mathematical model of a multilayer bimorph flapper in a double-nozzle flapper servo valve was conducted by Sedziak. The static and dynamic characteristics of multilayer bimorph in a double-nozzle flapper servo valve was tested by Zhu.[24] A control model of bimorph was built to reduce hysteresis by Milecki.[25] With influence of hydraulic fluids taken into account, the dynamic model of multilayer bimorph in a double-nozzle flapper servo valve was established by Chen.[26] These studies provide guidance for the modeling and simulation of multilayer bimorph, but are not very applicable to multilayer bimorph and deflector-feedback rod assembly in deflector jet servo valve due to different structure and working principle.

In deflector jet servo valves, the multilayer bimorph must actuate an irregularly-shaped connecting part and a deflector-feedback rod assembly which comprising a flexible rod with precision-aligned end balls. To address challenges of precisely driving flexible loads with complex structure, a mathematical model and nonlinear dynamic model for multilayer bimorph and deflector-feedback rod assembly in a deflector jet servo valve was conducted by Sangiah.[27] The structure directly reduced the moment of inertia while sacrificed post-assembly adjustability between multilayer bimorph and deflector-feedback rod. The model reflects the deflector center displacement and the feedback rod ball center displacement well while the feedback rod ball is free. However, the model relies on the EulerBernoulli beam theory, failing to account for the anticlastic deformation of multilayer bimorph[28,29] which is curvature along the width direction induced by bending along the length direction while the feedback rod ball is limited. Since the traditional model treats feedback force acted on the feedback rod ball as an externally prescribed input parameter of the assembly, and real-time monitoring of feedback force during whole valve operation is impractical, the traditional model cannot adequately characterize the correlation between assembly structural parameters, fitting clearance and output parameters.

To investigate multilayer bimorph performance under complex structural loads and precision driving conditions, a novel assembly structure is proposed firstly. Then the mathematical model of the assembly especially for limited feedback rod ball is conducted. Considering the effects of multilayer bimorph anticlastic deformation on force and displacement transmission, the parameters of model are identified through finite element analysis. The accuracy of model is verified by experiments and the static characteristics of the assembly are analyzed. The contribution of this work is twofold:

(1) A novel piezoelectric actuator for deflector jet servo valves is developed. The design offers adjustable bimorph clamping length and adjustable relative positioning between bimorph and feedback rod. These features enable optimization while maintaining stable, secure connections and minimizing moment of inertia.
(2) The static and dynamic mathematical model of the multilayer bimorph and deflector-feedback rod assembly is conducted, accounting for the anticlastic deformation of multilayer bimorph and limited feedback rod ball through the introduction of amendment coefficients. The model mainly characterizes the relationships between deflector center displacement, resistant force generated on feedback rod ball, hydraulic force acting on the deflector, and control voltage. By enabling precise calculation of the feedback force and deflector displacement, the models facilitate assessments: detecting assembly end fitting clearance and ensuring proper feedback force transmission, which are essential for maintaining linear displacement output and overall system reliability.
(3) Based on proposed models, analysis reveals how parameters (such as bimorph unclamping length) influence assembly output characteristics, with special emphasis on assembly end fitting clearance. These validated models provide a practical design tool that supports assembly optimal design under complex loading conditions, enabling performance optimization in engineering applications to be gained through the design of parameters like the optimal clearance range. These also provide theoretical support for developing precise valve control algorithms incorporating mechanical feedback.

The rest of this paper is organized as follows. The structure and working principle of the first stage assembly exposing the feedback rod are introduced in section 2. The static and dynamic mathematical mode of multilayer bimorph and deflector-feedback rod assembly is carried out in section 3. In section 4, parameter identification of the mathematical model is conducted. In

section 5, a prototype of the first stage assembly exposing the feedback rod is used in experiments under different working conditions to verify the model accuracy. In section 6, discussion is made. Finally, section 7 ends with some conclusions.

Structure and working principle

A cutaway of the first stage assembly exposing the feedback rod is composed of cover, polytetrafluoroethylene (PTFE) block, upper shell, fixing screw, multilayer bimorph (operating within a control voltage range of $\pm$ 100 V), set screw, connecting part and deflector-feedback rod, as shown in Figure 1(a). The main structure is multilayer bimorph and deflector-feedback rod assembly composed of multilayer bimorph and deflector-feedback rod. Figure 1(b) to (d) illustrates the assembly working states under zero, negative, and positive control voltages respectively.

The cover is connected to the upper shell with fixing screws. The multilayer bimorph functions as a cantilever beam. Bimorph fixed end is clamped to the upper shell through PTFE blocks preloaded by set screws, and the free end is connected to the deflector-feedback rod through connecting part with set screws. The deflector-feedback rod and connecting parts are assembled with an interference fit, ensuring elimination of relative movement. The end fixture, fabricated from photosensitive resin through 3D printing, incorporates an inclined-plane clamping mechanism that limit the movement of feedback rod ball.

The working principle of multilayer bimorph and deflector-feedback rod assembly: (1) When the control voltage is zero, the multilayer bimorph and deflector-feedback rod assembly is in the middle position and does not deflect; (2) When the control voltage is negative, the multilayer bimorph is deflected to the right and drives the deflector-feedback rod to be deflected to the right; (3) When the control voltage is positive, the multilayer bimorph is deflected to the left and drives the deflector-feedback rod to be deflected to the left.

Mathematical model

Based on the constitutive equation of piezoelectric effect,[30–32] Euler-Bernoulli beam theory, Hooke's law,[33] the overall mathematical modeling approach is illustrated in Figure 2.

The mathematical model of the assembly end displacement free feedback rod ball is established based on the model of multilayer bimorph end displacement, considering effects of coupling the connecting part and deflector-feedback rod on the output characteristics. The model of deflector center displacement for limited feedback rod ball is built based on the model of end displacement for free feedback rod ball, considering effects of reduction of effective driving force caused by bimorph anticlastic deformation and other effects.

Mathematical model of multilayer bimorph end displacement

The model of a single multilayer bimorph end displacement forms the foundation for subsequent modeling, with particular emphasis on bimorph end displacement. This model enables evaluation of how the multilayer bimorph unclamped length effects its end displacement.

Static model. The deflection of multilayer bimorph is shown in Figure 3.

When multilayer bimorph is not deflected, the multilayer bimorph exhibits infinite radius of curvature

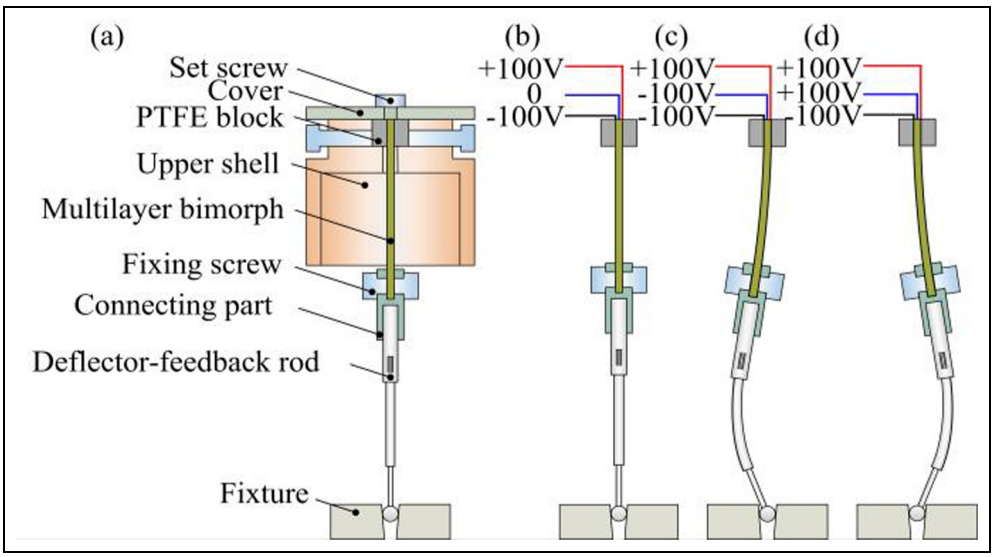

Figure 1. Structure and working states of the first stage: (a) structure, (b) working state when control voltage is zero, (c) working state when control voltage is negative, and (d) working state when control voltage is positive.

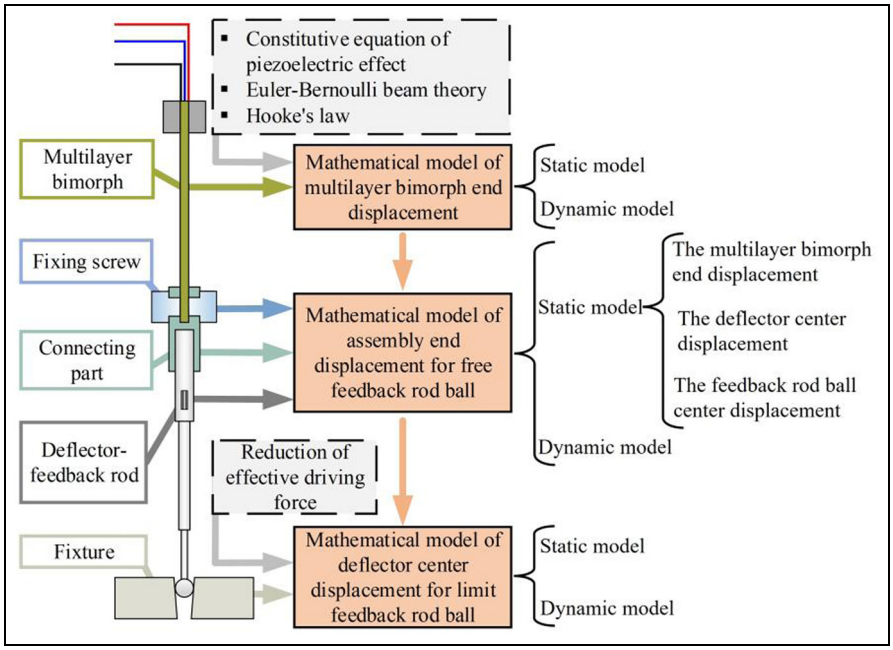

Figure 2. The overall mathematical modeling scheme of the assembly.

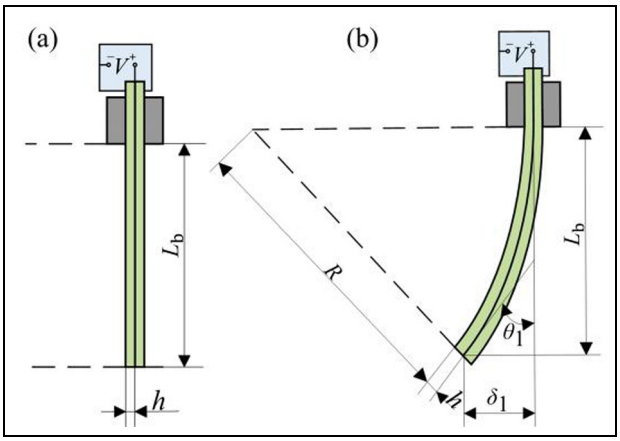

Figure 3. Schematic diagram of multilayer bimorph deflection: (a) when bimorph is not deflected and (b) when bimorph is deflected.

($R \to \infty$) and zero rotation angle ($\theta_1 = 0$). The bending moment and radius of curvature can be expressed as:

$$\frac{1}{R} = \frac{M_1}{E_b I_b} \tag{1}$$

where M_1 is the bending moment of bimorph when control voltage is applied and external force is zero; E_b is the Young's modulus of bimorph; and I_b is the cross-sectional inertia of bimorph.

Considering the bending caused by the inverse piezoelectric effect, the moment M_1 can be expressed as:

$$M_1 = \sigma b h^2 \tag{2}$$

where σ is the stress of bimorph; b is bimorph width; h is half thickness of multilayer bimorph.

The stress σ can be expressed as:

$$\sigma = d_{31} e E_b \tag{3}$$

where d_{31} is strain constant of piezoelectric materials; e is electric field strength.

The electric field strength e can be expressed as:

$$e = \frac{V}{\frac{h}{n_1}} = \frac{n_1 V}{h} \tag{4}$$

where V is control voltage amplitude; n_1 is half of bimorph layers.

The cross-sectional inertia of the multilayer bimorph I_b can be expressed as:

$$I_b = \frac{b(2h)^3}{12} = \frac{2bh^3}{3} \tag{5}$$

Substituting equations (2)–(5) into equation (1) gives:

$$R = \frac{2h^2}{3 n_1 d_{31} V} \tag{6}$$

As shown in Figure 4, the multilayer bimorph end displacement δ_1 can be expressed as:

$$\delta_1 = R(1 - \cos\theta_1) \tag{7}$$

where θ_1 is the cross-section deflection angle.

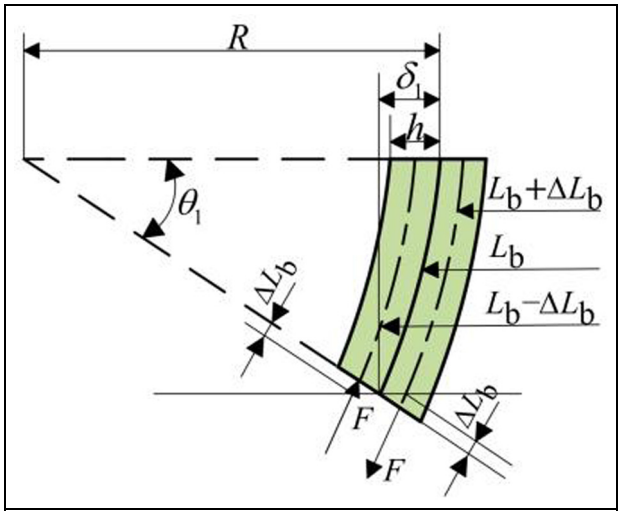

Figure 4. Structural parameters of deflected multilayer bimorph.

As deflection angle θ_1 of the multilayer bimorph tends to zero, cos θ can be seemed as $1–\theta^2/2$. The equation (7) can be simplified as:

$$\delta_1 = \frac{R\theta_1^2}{2} \tag{8}$$

As deflection angle of the multilayer bimorph tends to zero, θ_1 can be seemed as $\tan\theta_1$, thus:

$$\theta_1 = \frac{L_b}{R} \tag{9}$$

where L_b is the unclamped length of multilayer bimorph.

Substituting equations (6) and (9) into equation (8) gives:

$$\delta_1 = \frac{3L_b^2 d_{31} n_1}{4h^2} V \tag{10}$$

Substituting equations (6) and (10) into equation (9) gives:

$$\theta_1 = \frac{3L_b d_{31} n_1}{2h^2} V \tag{11}$$

Dynamic model. The multilayer bimorph is clamped as a cantilever beam. The active torque is generated by the control voltage which is mainly used to overcome the inertial moment, viscous moment and elastic moment of the multilayer bimorph. Combining equations (2)–(4), the dynamic model of a single multilayer bimorph can be expressed as follows:

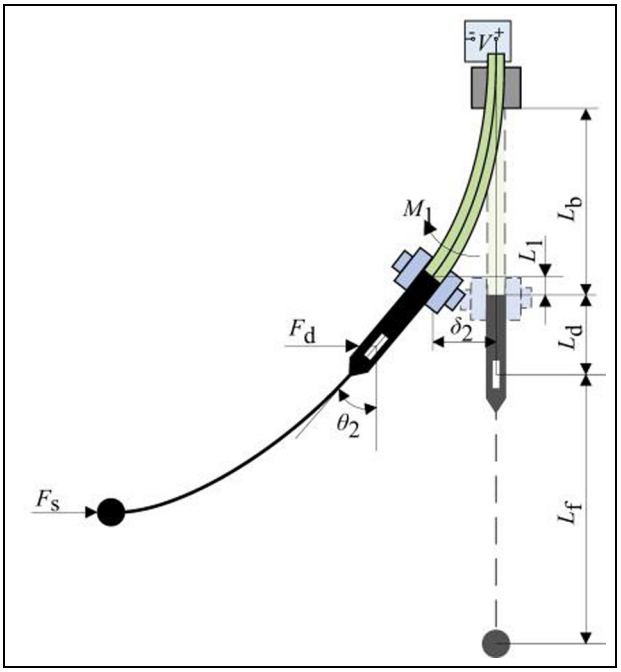

Figure 5. Schematic diagram of the multilayer bimorph end displacement.

$$J_1 \frac{d^2\theta_1}{dt^2} + C_1 \frac{d\theta_1}{dt} + K_1\theta_1 = d_{31} n_1 E_b bh \cdot V \tag{12}$$

where J_1 is the moment of inertia of the multilayer bimorph, which is only related to the size of the multilayer bimorph; C_1 is the damping coefficient of the rotation of the assembly, which is related to the moving medium; K_1 is stiffness of multilayer bimorph.

The stiffness of multilayer bimorph K_1 can be expressed as:

$$K_1 = \frac{M_1}{\theta_1} = \frac{2E_b bh^3}{3L_b} \tag{13}$$

Mathematical model of assembly end displacement for free feedback rod ball

In a deflector jet servo valve, the multilayer bimorph functions for driving deflector-feedback rod. Then the deflector center displacement directly effects the output characteristics of whole valve. As the feedback rod is an elastomer and the geometry of the connecting part is irregular, this study focuses on the deflector center displacement in the assembly, enables evaluation of how structural parameters of the assembly effects deflector center displacement and feedback rod ball trajectory.

Static model. a. The multilayer bimorph end displacement. The multilayer bimorph end displacement δ_2 in assembly is shown in Figure 5.

According to the Euler-Bernoulli beam theory, the end displacement δ_2 can be expressed as:

$$\delta_2 = \frac{WL_b^3}{3E_bI_b} + \frac{M_2L_b^2}{2E_bI_b} \tag{14}$$

where W is multilayer bimorph end force; M_2 is multilayer bimorph end bending moment.

The deflection angle θ_2 of the deflector section can be expressed as:

$$\theta_2 = \frac{WL_b^2}{2E_bI_b} + \frac{M_2L_b}{E_bI_b} \tag{15}$$

According to the translational theorem of force, the end force W and moment M_2 can be expressed as:

$$M_2 = M_1 - (L_d + L_f)F_s - L_dF_d \tag{16}$$

$$W = -(F_s + F_d) \tag{17}$$

where L_d is the distance between the deflector center and the multilayer bimorph end; L_f is the length of feedback rod; F_s is the resistant force generated on the feedback rod which equals to the feedback force acted on the feedback rod ball; F_d is the hydraulic force acting on the deflector.

Solving simultaneous equations (2)–(4) and (14)–(17) gives:

$$\delta_2 = \frac{3L_\mathrm{b}^2d_{31}n_\mathrm{l}V}{4h^2} - \frac{L_\mathrm{b}^2}{6E_\mathrm{b}I_\mathrm{b}}[2L_\mathrm{b}(F_\mathrm{s} + F_\mathrm{d}) + 3F_\mathrm{s}(L_\mathrm{d} + L_\mathrm{f}) + 3L_\mathrm{d}F_\mathrm{d}] \tag{18}$$

$$\theta_2 = \frac{3d_{31}L_\mathrm{b}n_\mathrm{l}V}{2h^2} - \frac{L_\mathrm{b}}{2E_\mathrm{b}I_\mathrm{b}}[L_\mathrm{b}(F_\mathrm{s} + F_\mathrm{d}) + 2F_\mathrm{s}(L_\mathrm{d} + L_\mathrm{f}) + 2L_\mathrm{d}F_\mathrm{d}] \tag{19}$$

The multilayer bimorph end displacement δ_2 and deflection angle θ_2 have been obtained in equations (18) and (19). In order to further determine the trajectory for free feedback rod ball, the axial multilayer bimorph displacement L_1 is:

$$L_1 = L_b - \delta_2\tan^{-1}\frac{\delta_2}{L_b} \tag{20}$$

Substituting equation (18) into (20) gives:

$$L_\mathrm{l} = L_b - \frac{\frac{3L_bd_{31}n_\mathrm{l}V}{4h^2} - \frac{L_b}{6E_\mathrm{b}I_\mathrm{b}}[2L_\mathrm{b}(F_\mathrm{s} + F_\mathrm{d}) + 3F_\mathrm{s}(L_\mathrm{d} + L_\mathrm{f}) + 3L_\mathrm{d}F_\mathrm{d}]}{\frac{3d_{31}n_\mathrm{l}V}{4h^2} - \frac{1}{4E_\mathrm{b}I_\mathrm{b}}[L_\mathrm{b}(F_\mathrm{s} + F_\mathrm{d}) + 2F_\mathrm{s}(L_\mathrm{d} + L_\mathrm{f}) + 2L_\mathrm{d}F_\mathrm{d}]} \tag{21}$$

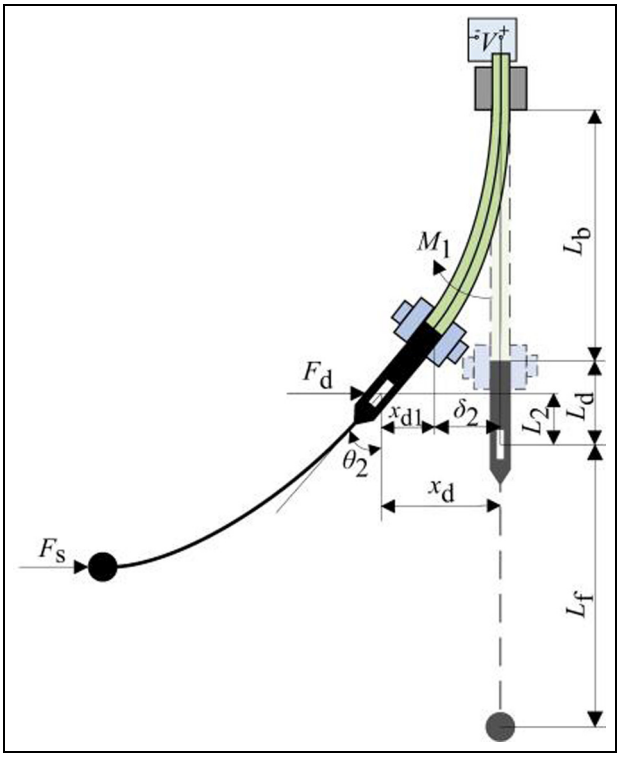

Figure 6. Schematic diagram of the deflector center displacement for free feedback rod ball.

b. The deflector center displacement. Assuming that the deflector is fixed to the bimorph end and ignoring the deflector deformation, the deflector center displacement x_d is shown in Figure 6.

The deflector center displacement x_d is:

$$x_\mathrm{d} = \delta_2 + x_\mathrm{d1} \tag{22}$$

where x_d1 is the displacement of deflector center relative to the multilayer bimorph end.

The deflector center displacement relative to the multilayer bimorph end x_d1 can be expressed as:

$$x_\mathrm{d1} = L_\mathrm{d}\sin\theta_2 \tag{23}$$

Since θ_2 is small enough, it can be equal to $\sin\theta_2$. Substituting equations (18), (19), and (23) into equation (22) gives:

$$x_\mathrm{d} = (L_\mathrm{b} + 2L_\mathrm{d})\frac{3L_\mathrm{b}d_{31}n_\mathrm{l}}{4h^2}V - \frac{L_\mathrm{b}}{2E_\mathrm{b}I_\mathrm{b}}\left[\frac{2L_\mathrm{b}^2}{3} + 2L_\mathrm{b}L_\mathrm{d} + 2L_\mathrm{d}^2\right]F_\mathrm{d} - \frac{L_\mathrm{b}}{2E_\mathrm{b}I_\mathrm{b}}\left[\frac{2L_\mathrm{b}^2}{3} + L_\mathrm{b}(L_\mathrm{d} + L_\mathrm{f}) + 2L_\mathrm{d}(L_\mathrm{d} + L_\mathrm{f}) + L_\mathrm{d}L_\mathrm{b}\right]F_\mathrm{s} \tag{24}$$

The deflector center displacement x_d has been obtained in equation (24). In order to further determine the trajectory for free feedback rod ball, the axial deflector center displacement L_2 is:

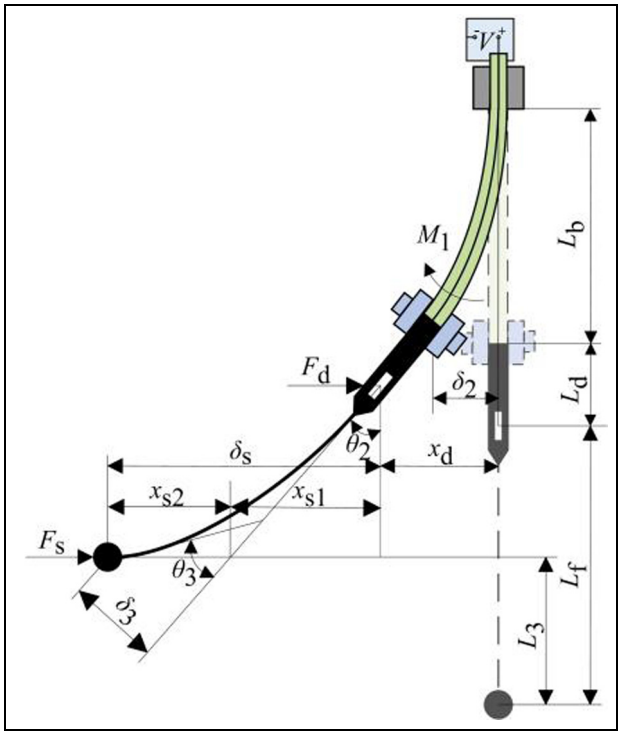

Figure 7. Schematic diagram of the feedback rod ball center displacement.

$$L_2 = L_1 + L_\mathrm{d}\cos\theta_2 \tag{25}$$

c. The feedback rod ball center displacement. The feedback rod ball center displacement x_s which can be seen as assembly end displacement is shown in Figure 7.

The feedback rod deflects following the Euler-Bernoulli beam theory. The feedback rod ball center displacement x_s can be expressed as:

$$x_\mathrm{s} = x_\mathrm{d} + \delta_\mathrm{s} \tag{26}$$

where δ_s is the feedback rod ball center displacement relative to the deflector center.

The feedback rod ball center displacement δ_s relative to deflector center can be expressed as:

$$\delta_\mathrm{s} = x_{\mathrm{s}1} + x_{\mathrm{s}2} \tag{27}$$

where $x_{\mathrm{s}1}$ is the feedback rod ball center displacement caused by multilayer bimorph deflection, $x_{\mathrm{s}2}$ is the feedback rod ball center deflection relative to the deflector center.

The feedback rod ball center displacement caused by multilayer bimorph deflection $x_{\mathrm{s}1}$ and the feedback rod ball center deflection the relative to the deflector center $x_{\mathrm{s}2}$ can be expressed as:

$$x_{s1} = \theta_2 L_\mathrm{f} \tag{28}$$

$$x_{s2} = \delta_3\cos^{-1}\theta_2 \tag{29}$$

Based on Euler-Bernoulli beam theory, the feedback rod ball center displacement δ_3 and feedback rod deflection angle θ_3 relative to the central axis of the deflector can be obtained that:

$$\delta_3 = \frac{1}{\tan\theta_2}\sqrt{\frac{E_\mathrm{f}I_\mathrm{f}}{F_s\theta_2}}\tan\left(L_\mathrm{f}\sqrt{\frac{F_s\theta_2}{E_\mathrm{f}I_\mathrm{f}}}\right) - \frac{L_\mathrm{f}}{\tan\theta_2} \tag{30}$$

$$\theta_3 = \frac{L_\mathrm{f}}{\theta_2}\left[2\sin\left(L_\mathrm{f}\sqrt{\frac{F_s\sin\theta_2}{E_\mathrm{f}I_\mathrm{f}}}\right) - 1\right] \tag{31}$$

where I_f is the cross-sectional moment of inertia of the feedback rod; E_f is the Young's modulus of feedback rod.

Substituting equations (19), (24), and (27)–(30) into equation (26), the feedback rod ball center displacement x_s is obtained as:

$$\begin{aligned} x_\mathrm{s} &= (L_\mathrm{b} + 2L_\mathrm{d} + 2L_\mathrm{f})\frac{3L_\mathrm{b}d_{31}n_\mathrm{l}}{4h^2}V \\ &- \frac{L_\mathrm{b}}{2E_\mathrm{b}I_\mathrm{b}}\left[\frac{2L_\mathrm{b}^2}{3} + 2L_\mathrm{b}L_\mathrm{d} + 2L_\mathrm{d}^2 + L_\mathrm{b}L_\mathrm{f} + 2L_dL_\mathrm{f}\right]F_\mathrm{d} \\ &- \left[\frac{L_\mathrm{b}}{E_\mathrm{b}I_\mathrm{b}}\left(\frac{L_\mathrm{b}^2}{3} + L_\mathrm{b}L_\mathrm{d} + L_\mathrm{b}L_\mathrm{f} + L_d^2 + 2L_\mathrm{d}L_\mathrm{f} + L_\mathrm{f}^2\right) + \frac{L_\mathrm{f}^3}{3E_\mathrm{f}I_\mathrm{f}}\right]F_\mathrm{s} \end{aligned} \tag{32}$$

The feedback rod ball center displacement x_s has been obtained in equation (32). In order to further determine the trajectory for free feedback rod ball, the axial feedback rod ball center displacement L_3 can be expressed as:

$$L_3 = L_2 + \cos\theta_2\left(L_\mathrm{f} - \delta_3\tan^{-1}\frac{\delta_3}{L_\mathrm{f}}\right) \tag{33}$$

Dynamic model. When the feedback rod ball is free, the main driving torque is the bending moment M_1 generated by the change of control voltage, which is mainly used to overcome the moment of inertia, viscous moment, elastic moment and the moment generated by the liquid flow force F_d on the multilayer bimorph and deflector-feedback rod assembly. The dynamic model is:

$$J_2\frac{\mathrm{d}^2\theta_2}{\mathrm{d}t^2} + C_2\frac{\mathrm{d}\theta_2}{\mathrm{d}t} + K_1\theta_2 = d_{31}n_\mathrm{l}E_\mathrm{b}bh\cdot V - F_\mathrm{d}L_\mathrm{d} \tag{34}$$

where J_2 is the moment of inertia of the assembly; C_2 is the damping coefficient of the rotation of the assembly, which is related to the moving medium.

Mathematical model of deflector center displacement for limited feedback rod ball

In practical working conditions, the feedback rod ball is limited. This model enables evaluation of how feedback rod ball fitting clearance effects deflector center displacement and feedback force acted on feedback rod ball, provides theoretical support for multilayer bimorph applications in complex structural load with end limitation.

The mathematical model of the multilayer bimorph and deflector-feedback rod assembly while the feedback rod ball is free is established in subsection 3.2. The traditional model while the feedback rod ball is limited is directly derived from the model while the ball is free, let the feedback rod ball center displacement is zero ($x_s = 0$). The relationship between the resistant force on the feedback rod ball F_s and the hydraulic force F_d can be directly derived:

$$F_s = \frac{(L_b + 2L_d + 2L_f)\frac{3L_b d_{31} n_1}{4h^2}}{\frac{L_b}{E_b I_b}\left(\frac{L_b^2}{3} + L_b L_d + L_b L_f + L_d^2 + 2L_d L_f + L_f^2\right) + \frac{L_f^3}{3E_f I_f}} V - \frac{\frac{L_b}{2E_b I_b}\left(\frac{2L_b^2}{3} + 2L_b L_d + 2L_d^2 + L_b L_f + 2L_d L_f\right)}{\frac{L_b}{E_b I_b}\left(\frac{L_b^2}{3} + L_b L_d + L_b L_f + L_d^2 + 2L_d L_f + L_f^2\right) + \frac{L_f^3}{3E_f I_f}} F_d \tag{35}$$

Substituting equation (35) into (24), the deflector center displacement can be obtained:

$$x_{dlim} = \frac{3L_b d_{31} n_1}{4h^2} \left[\frac{-\frac{1}{6}L_b^2 L_f + \frac{E_b I_b L_f^3}{3E_f I_f L_b}(L_b + 2L_d)}{\left(\frac{L_b^2}{3} + L_b L_d + L_b L_f + L_d^2 + 2L_d L_f + L_f^2\right) + \frac{E_b I_b L_f^3}{3E_f I_f L_b}}\right] V - \frac{L_b}{2E_b I_b} \left[\frac{\frac{1}{6}L_b^2 L_f^2 + \frac{E_b I_b L_f^3}{3E_f I_f L_b}\left(\frac{2L_b^2}{3} + 2L_b L_d + 2L_d^2\right)}{\left(\frac{L_b^2}{3} + L_b L_d + L_b L_f + L_d^2 + 2L_d L_f + L_f^2\right) + \frac{E_b I_b L_f^3}{3E_f I_f L_b}}\right] F_d \tag{36}$$

However, the bimorph anticlastic deformation becomes greater when the feedback rod ball is limited. leading to a reduction in effective driving force. The traditional model neglects cross sectional deformation resulting in overestimated displacement while the feedback rod ball is limited, and also introduces significant deflection displacement errors due to error accumulation. To address these limitations, a mathematical model of deflector center displacement is revised.

Static model. The schematic diagram of the assembly for limited feedback rod ball is shown in Figure 8.

Based on constitutive equation of piezoelectric effect, the relationships among control voltage, the multilayer bimorph end displacement and the bimorph end output force can be expressed as:

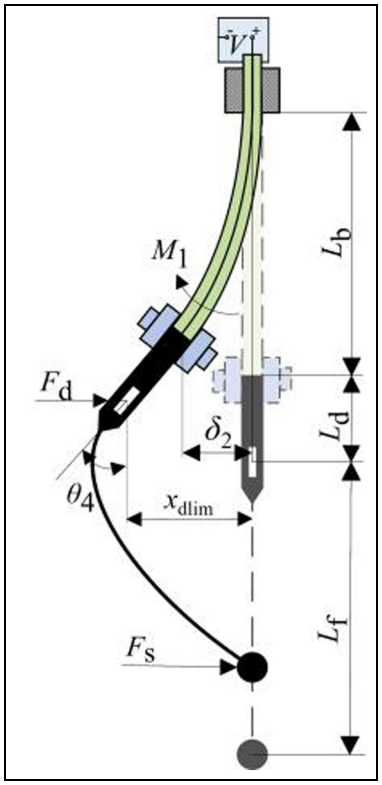

Figure 8. Schematic diagram of deflector center displacement for limited feedback rod ball.

$$\delta_2 = \frac{n_1 L_b^3}{2bE_b h^3} F_{equal} - \frac{3n_1 d_{31} L_b^2}{4h^2} V \tag{37}$$

where δ_2 is the multilayer bimorph end displacement, and F_{equal} is the bimorph output force.

Based on moment balance equation, the bimorph end output force F_{equal} can be expressed as:

$$F_{equal} = \frac{F_s(L_b + L_d + L_f) + F_d(L_b + L_d)}{L_b} \tag{38}$$

Substituting equations (18) and (38) into (37), the resistant force on the feedback rod ball F_s can be expressed as:

$$F_s = \frac{3n_1 E_b d_{31} L_b}{\frac{n_1 L_b}{bh}(L_b + L_d + L_f) + \frac{h^2}{I_b}\left[\frac{2L_b^2}{3} + L_b L_f + L_d L_b\right]} V - \frac{\frac{n_1 L_b}{bh^3}(L_b + L_d) + \frac{1}{I_b}(\frac{2L_b^2}{3} + L_b L_d)}{\frac{n_1 L_b}{bh^3}(L_b + L_d + L_f) + \frac{1}{I_b}\left[\frac{2L_b^2}{3} + L_b L_f + L_d L_b\right]} F_d \tag{39}$$

Substituting equations (39) into (24), the deflector center displacement x_{dlim} can be obtained:

$$x_{\mathrm{dlim}} = \frac{3n_1 d_{31} L_{\mathrm{b}}}{2} \left[\frac{(L_{\mathrm{b}} + 2L_{\mathrm{d}})}{2h^2} - \frac{\frac{2L_{\mathrm{b}}^2}{3} + 2L_{\mathrm{b}}L_{\mathrm{d}} + L_{\mathrm{b}}L_{\mathrm{f}} + 2L_{\mathrm{d}}^2 + 2L_{\mathrm{d}}L_{\mathrm{f}}}{\frac{n_1 I_{\mathrm{b}}}{bh}(L_{\mathrm{b}} + L_{\mathrm{d}} + L_{\mathrm{f}}) + h^2\left(\frac{2L_{\mathrm{b}}}{3} + L_{\mathrm{f}} + L_{\mathrm{d}}\right)} \right] V + \frac{1}{2E_{\mathrm{b}} I_{\mathrm{b}}} \frac{\frac{n_1 L_{\mathrm{b}}}{bh^3}\left[\frac{L_{\mathrm{b}}^2 L_{\mathrm{f}}}{3} + L_{\mathrm{b}}L_{\mathrm{d}}L_{\mathrm{f}}\right] + \frac{L_{\mathrm{b}}^2 L_{\mathrm{d}} L_{\mathrm{f}}}{3I_{\mathrm{b}}}}{\frac{n_1}{bh^3}(L_{\mathrm{b}} + L_{\mathrm{d}} + L_{\mathrm{f}}) + \frac{1}{I_{\mathrm{b}}}\left[\frac{2L_{\mathrm{b}}}{3} + L_{\mathrm{f}} + L_{\mathrm{d}}\right]} F_{\mathrm{d}} \tag{40}$$

In the model above, we consider the connecting part as a rigid body. However, in practical, a part of the multilayer bimorph output power is used for connecting part deformation and bimorph anticlastic deformation. As shown in subsection 4.2, discrepancies exist between this model above (equations (39) and (40)) and finite element simulation results, with maximum relative errors of 24.5% for resistant force and 36.5% for deflector center displacement.

The actual anticlastic deformation of the bimorph crosssection and deformations of the connecting part are complex. Considering the linear relationship between feedback force and deflector displacement, we propose two amendment coefficients: λ for the increase of bimorph end output force; γ for displacement reduction from reduction of effective driving force. The feedback force acted on the feedback rod ball F_{s} can be expressed as:

$$F_{\mathrm{s}} = \frac{3n_1 E_{\mathrm{b}} d_{31} L_{\mathrm{b}}}{\frac{n_1 L_{\mathrm{b}}}{bh}(L_{\mathrm{b}} + L_{\mathrm{d}} + L_{\mathrm{f}}) + \frac{h^2}{I_{\mathrm{b}}}\left[\frac{2L_{\mathrm{b}}^2}{3} + L_{\mathrm{b}}L_{\mathrm{f}} + L_{\mathrm{d}}L_{\mathrm{b}}\right]} V - \frac{\frac{n_1 L_{\mathrm{b}}}{bh^3}(L_{\mathrm{b}} + L_{\mathrm{d}}) + \frac{1}{I_{\mathrm{b}}}\left(\frac{2L_{\mathrm{b}}^2}{3} + L_{\mathrm{b}}L_{\mathrm{d}}\right)}{\frac{n_1 L_{\mathrm{b}}}{bh^3}(L_{\mathrm{b}} + L_{\mathrm{d}} + L_{\mathrm{f}}) + \frac{1}{I_{\mathrm{b}}}\left[\frac{2L_{\mathrm{b}}^2}{3} + L_{\mathrm{b}}L_{\mathrm{f}} + L_{\mathrm{d}}L_{\mathrm{b}}\right]} F_{\mathrm{d}} - \lambda x_{\mathrm{d}} \tag{41}$$

The deflector center displacement x_{dlim} can be expressed as:

$$x_{\mathrm{dlim}} = (L_{\mathrm{b}} + 2L_{\mathrm{d}})\frac{3L_{\mathrm{b}} d_{31} n_{\mathrm{l}}}{4h^2} V - \frac{L_{\mathrm{b}}}{2E_{\mathrm{b}} I_{\mathrm{b}}}\left[\frac{2L_{\mathrm{b}}^2}{3} + 2L_{\mathrm{b}}L_{\mathrm{d}} + 2L_{\mathrm{d}}^2\right] F_{\mathrm{d}} - \frac{L_{\mathrm{b}}}{2E_{\mathrm{b}} I_{\mathrm{b}}}\left[\frac{2L_{\mathrm{b}}^2}{3} + L_{\mathrm{b}}(L_{\mathrm{d}} + L_{\mathrm{f}}) + 2L_{\mathrm{d}}(L_{\mathrm{d}} + L_{\mathrm{f}}) + L_{\mathrm{d}}L_{\mathrm{b}}\right] F_{\mathrm{s}} + \gamma F_s \tag{42}$$

The amendment coefficients are identified through Isight based on finite element analysis through COMSOL in subsection 4.2.

Dynamic model. Considering the limited the feedback rod ball, the active moment also needs to overcome the moment formed by the feedback force acted on the feedback rod ball. The dynamic model is:

$$J_2 \frac{\mathrm{d}^2\theta_4}{\mathrm{dt}^2} + C_2 \frac{\mathrm{d}\theta_4}{\mathrm{dt}} + K_2\theta_4 = d_{31} n_{\mathrm{l}} E_{\mathrm{b}} bh \cdot V - F_{\mathrm{d}} L_{\mathrm{d}} - F_{\mathrm{s}}(L_{\mathrm{d}} + L_{\mathrm{f}}) \tag{43}$$

Parameter identification

The mathematical model requires identification of two coefficient of amendments: λ for the increase of bimorph end output force in equation (41); γ for displacement reduction from reduction of effective driving force in equation (42). The model of the multilayer bimorph and deflector-feedback rod assembly is developed in Matlab/Simulink firstly. The amendment coefficients are then identified in Isight.

The mathematical model of assembly built in MATLAB/Simulink

Based on the established mathematical model of multilayer bimorph and deflector-feedback rod assembly, a simulation model of the assembly is established in MATLAB/Simulink, as shown in Figure 9. The model is built based on the MATLAB Function module.

For free feedback rod ball, the main input signals are the control voltage, feedback force acted on the feedback rod ball, liquid flow force acted on the deflector; the main output signals are deflector center displacement and feedback rod ball center displacement. While the feedback rod ball is limited, the main input signals are the control voltage, liquid flow force acted on the deflector; the main output signals are deflector center displacement and resistant force generated on the feedback rod ball. The main simulation parameters of the assembly are shown in Table 1.

Identification of amendments coefficients

Using COMSOL for finite element analysis of assembly, the deflector center displacement and the resistant force generated on the feedback rod ball in air can be obtained. The density, elastic modulus, and Poisson's ratio of different parts in the assembly are shown in Table 2.

In practical valve operation, the feedback rod ball is permitted a limited amount of axial displacement. As this is very small compared to deflection of feedback rod ball center, the axial displacement is neglected in the following simulations. Based on finite element analysis in COMSOL, when the frequency of the continuous sinusoidal control voltage is 0.1 Hz and amplitude is 100 or 40 V, the continuous deflector center displacement and the resistant force generated on the feedback rod ball can be obtained. The surface stress of the multilayer bimorph when achieving the

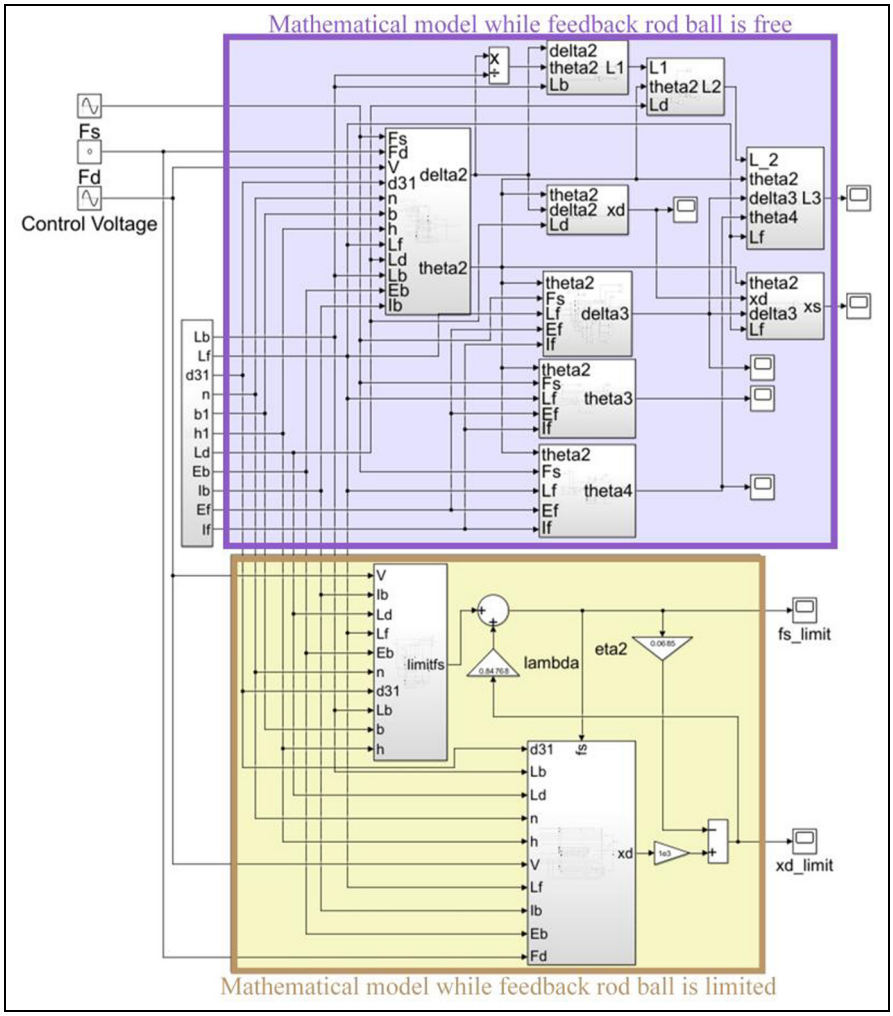

Figure 9. Mathematical model of the assembly.

Table 1. Main parameters of the assembly.

Name	Symbol	Value	Units
Piezoelectric constant[34]	d_{31}	1.95×10^{-10}	C/N
The unclamped length of multilayer bimorph	L_b	16.50×10^{-3}	m
Half thickness of multilayer bimorph[35]	h	0.65×10^{-3}	m
The width of multilayer bimorph	b	7.80×10^{-3}	m
The moment of inertia of feedback rod	I_f	2.80×10^{-13}	m^4
Young's modulus of multilayer bimorph	E_b	6.25×10^{10}	N/m^2
The moment inertia of multilayer bimorph	I_b	1.43×10^{-12}	m^4
The length of deflector	L_d	9.23×10^{-3}	m
The length of feedback rod	L_f	18.08×10^{-3}	m
Young's modulus of feedback rod	E_f	1.80×10^{11}	N/m^2
Half layers of the piezoelectric ceramic	n	9	-

Table 2. The main material parameters of the assembly.

Name of each part	Density (kg/m^3)	Elastic modulus (N/m^2)	Poisson's ratio
Multilayer bimorph	7.85×10^3	6.0×10^{10}	0.32
Fixing screw	7.90×10^3	2.0×10^{11}	0.28
Connecting part	2.80×10^3	7.0×10^{10}	0.33
Deflector-feedback rod	8.80×10^3	1.2×10^{11}	0.35

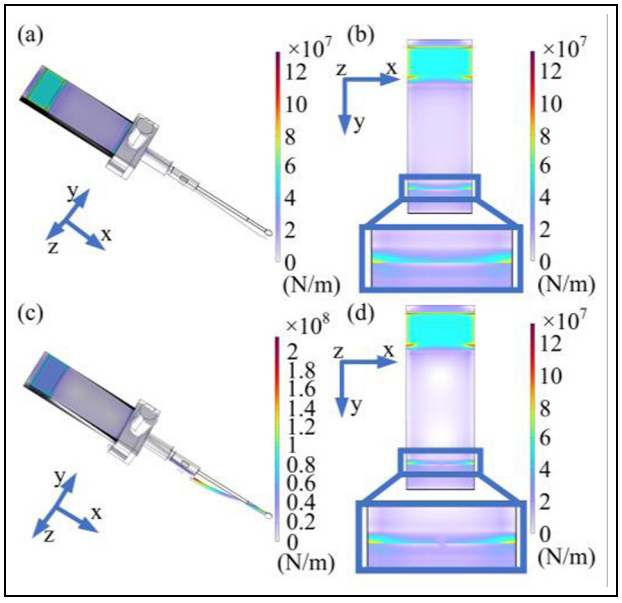

Figure 10. Stress while the control voltage amplitude is 100 V: (a) assembly while ball is free, (b) bimorph surface stress while ball is free, (c) the assembly while ball is limited, and (d) bimorph surface stress while ball is limited.

maximum deflection is extracted, as shown in Figure 10(b) and (d).

The stress on both sides of contact boundary on bimorph between the surface of the multilayer bimorph and the connecting part is relatively higher, while there is a noticeable area in the middle with significantly lower stress. Especially for limited feedback rod ball, there is very little stress at the center of the contact boundary between the bimorph surface and the connecting part, indicating anticlastic deformation is existed. Through Isight, minimize both maximum absolute error and root mean square error between mathematical model results and finite analysis, with priority given to reducing the maximum absolute error.[36–38] Solve for 3375 sets of amendment coefficients to obtain the optimal one.

According to the identification in Isight, gives that λ is 847.68, γ is 6.85×10^{-5} while output force is in newtons and deflector displacement is in meters. The comparison among the results of the mathematical models whether there are amendments or not and the results of finite element analysis in COMSOL can be seen in Figure 11.

Experimental validations

The experimental validations comprise two parts: the first part is to test the resistant force generated on feedback rod ball and deflector center displacement in air conditions, and compare the experimental results with the mathematical results; the second part is to test of the deflector center displacement in oil or air whether the feedback rod ball is limited or not, and compare the experimental results with the mathematical results for each operational condition.

Experiment on the resistant force and deflector center displacement in air

In order to achieve the purpose of testing the deflector center displacement and the resistant force generated on feedback rod ball, an experimental platform was first built. The experimental system consists of six parts: power amplifier, fixture, assembly, laser sensor, and force sensor, as shown in Figure 12. The supervisory computer generates a sinusoidal continuous signal, which is then amplified by power amplifier before being applied to the multilayer bimorph. The deflector center displacement is measured by laser sensor; the resistant force is measured by force sensor. An initial force is applied to ensure that the feedback rod ball cannot detach from force sensor.

The control voltage amplitudes are set to 30, 50, and 80 V respectively, with frequency of 0.1 Hz. Compare the results of the mathematical model with amendments (equations (41) and (42)), model derived directly (equations (35) and (36)) with experimental results, as shown in Figure 13.

Compared with the model derived directly, simulation results of the mathematical model with amendments are more similar to the experimental results. Based on the experimental results obtained, the maximum absolute error, mean absolute error, root mean square error of mathematical models are shown in Table 3.

As shown in Table 3, the errors of mathematical model with amendments have significantly reduced compared with traditional model (derived directly); the relative error in deflector center displacement tends to increase with higher control voltage indicating that hysteresis exerts a stronger influence under larger control voltage. Considering the hysteresis is existed in experimental results, the errors of the peak-to-peak values of the output force and output displacement are shown in Table 4.

As shown in Table 4, the errors of peak-to-peak values of mathematical model with amendments have significantly reduced compared with traditional model (derived directly); the proposed model exhibits larger relative error at lower voltage. As for the mathematical model with amendments compared with experimental results, the maximum relative error of output force is 9.68%, the maximum relative error of deflector displacement is 14.46% Although amendments enhance the predictive capability of the model while the feedback rod ball is limited, it does not fully capture the physical effects at lower voltages.

The proposed model may lose accuracy under conditions where the control voltage amplitude is quite low;

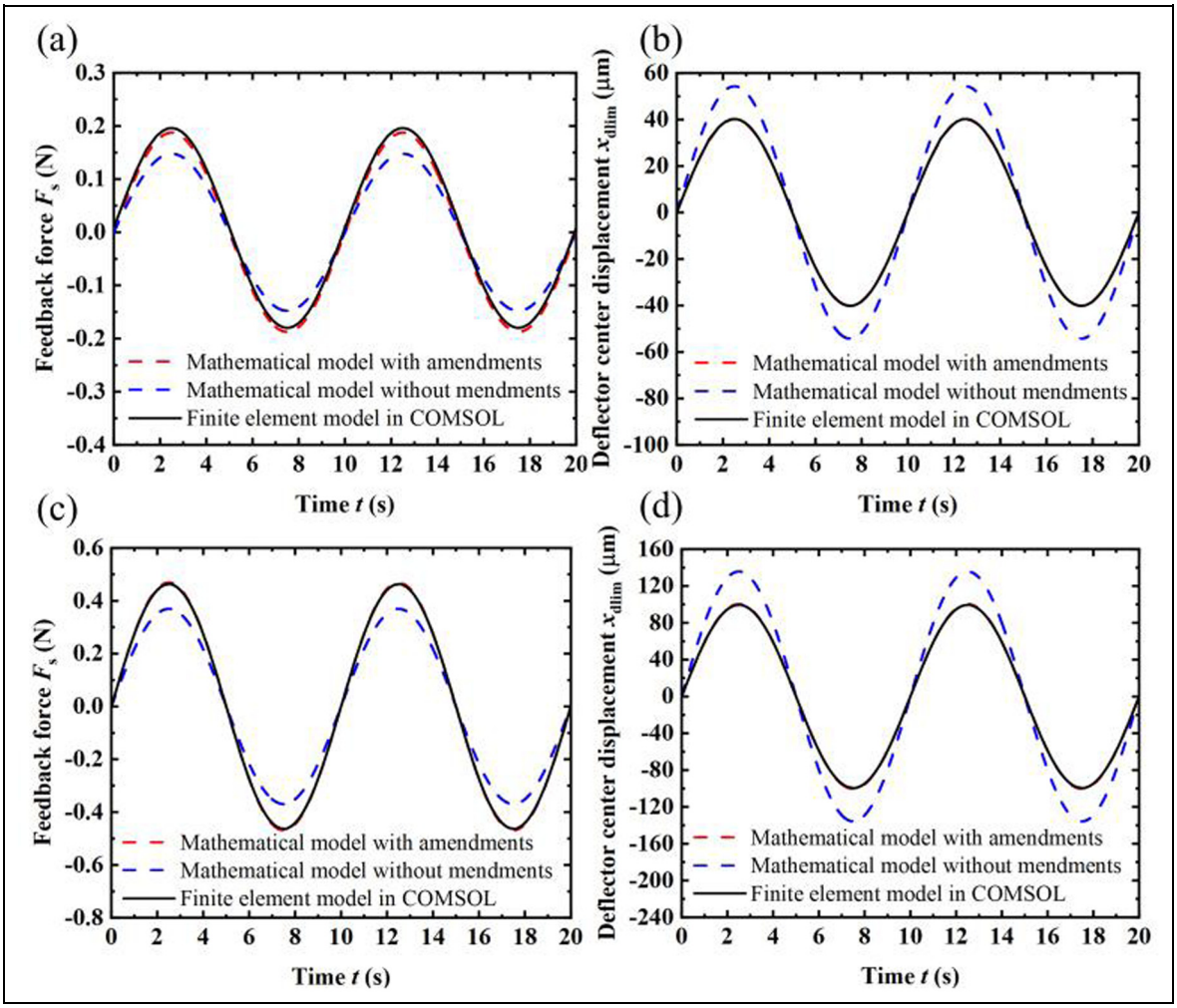

Figure 11. Comparison among results of mathematical models and finite element model: (a) output force while control voltage is 40 V, (b) deflector displacement while control voltage is 40 V, (c) output force while control voltage is 100 V, (d) deflector displacement while control voltage is 100 V.
The simulation results of the mathematical model with amendments are more similar to the finite element analysis in COMSOL.

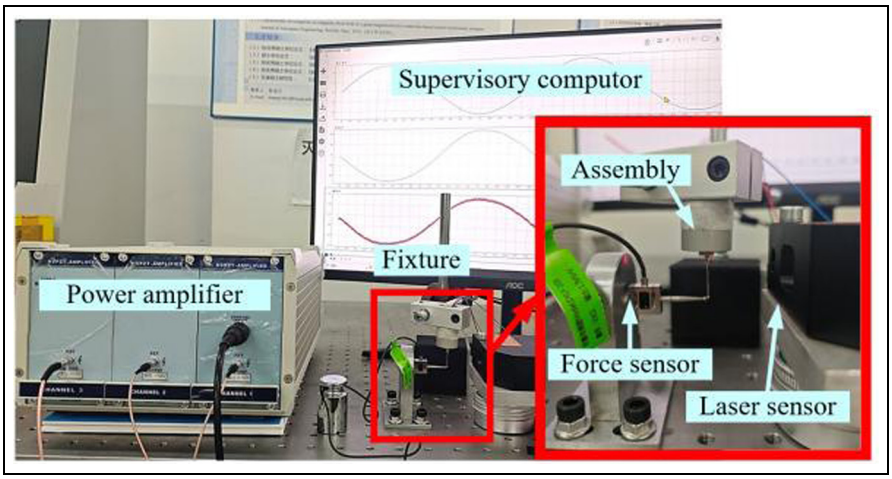

Figure 12. Testing platform of resistant force and deflector center displacement.

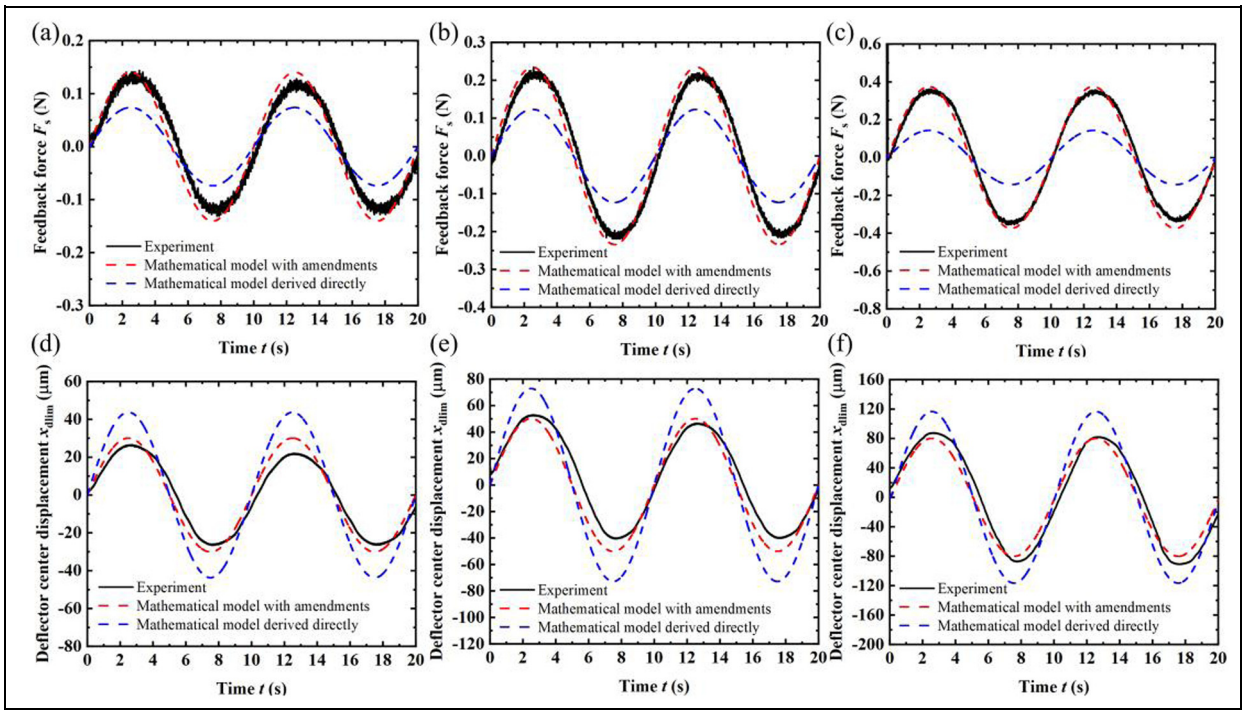

Figure 13. The comparison among results of mathematical model and experiment: (a) force while control voltage amplitude is 30 V, (b) force while control voltage amplitude is 50 V, (c) force while control voltage amplitude is 80 V, (d) displacement while control voltage amplitude is 30 V, (e) displacement while control voltage amplitude is 50 V, and (f) displacement while control voltage amplitude is 80 V.

Table 3. The error between the mathematical result curve and the experimental result curve.

		Maximum absolute error		Mean absolute error		Root mean square error	
Control voltage (V)	Parameters	With amendments	Derived directly	With amendments	Derived directly	With amendments	Derived directly
30	F_s/N	0.040	0.060	0.020	0.032	0.022	0.035
50	F_s/N	0.053	0.110	0.026	0.062	0.028	0.068
80	F_s/N	0.067	0.220	0.027	0.130	0.028	0.150
30	x_{dlim}/μm	8.92	22.31	4.77	12.53	4.96	13.96
50	x_{dlim}/μm	13.99	25.48	6.77	15.78	6.98	17.00
80	x_{dlim}/μm	19.54	36.03	11.56	22.05	12.67	24.24

Table 4. The error of peak-to-peak values between the mathematical results and the experimental results.

		Absolute error		Relative error (%)	
Control voltage (V)	Parameters	With amendments	Derived directly	With amendments	Derived directly
30	F_s	0.025 N	0.093 N	9.68	38.64
50	F_s	0.034 N	0.180 N	7.85	42.10
80	F_s	0.056 N	0.400 N	8.03	58.53
30	x_{dlim}	7.60 μm	38.98 μm	14.46	80.46
50	x_{dlim}	7.29 μm	27.27 μm	7.84	15.76
80	x_{dlim}	12.36 μm	60.14 μm	7.15	34.77

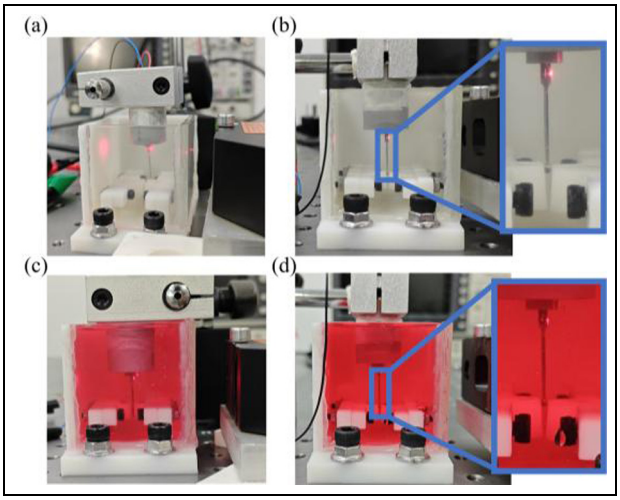

Figure 14. Partial testing device: (a) while the feedback rod ball is free in air, (b) while the feedback rod ball is limited in air, (c) while the feedback rod ball is free in oil, and (d) while the feedback rod ball is limited in oil.

where significant deformation occurs in the connecting part; where the hysteresis of the bimorph becomes influential.

Experiment on deflector center displacement under different working conditions

Based on testing platform of deflector center displacement and the resistant force generated on feedback rod ball, extend the assembly into the transparent container. The deflector center displacement is measured by laser sensor. The partial testing device is shown in the Figure 14.

The control voltage amplitude is 50 V, the frequency is 0.1 Hz. In Figure 15(a), the experimental results whether the feedback rod ball is limited or not in oil and air are compared with simulations from the proposed model. Figure 15(b) compares the experimental results while the feedback rod ball is free in oil and air with the simulation results of both the proposed and traditional models. Figure 15(c) compares the experimental results while the feedback rod ball is limited in oil and air with the simulation results of both the proposed and traditional models.

The experimental peaktopeak values of the deflector center displacement in oil and air differ by no more than 4%. While the feedback rod ball is free in air, both the traditional model (derived directly) and our proposed model agree well with experimental results, with maximum peak-to-peak errors below 3%. While the feedback rod ball is limited in air, the traditional model yields a maximum error of 45.7%, while our proposed model reduces this error to 4.7%. Notably, significant curve deviations occur near 4.6 and 14.6 s, attributable to measurement point shift after the light is refracted by the oil flow caused by assembly movement.

Discussion

Based on model of single multilayer bimorph end displacement δ_1 (equation (10)), the effect of multilayer bimorph unclamped length on bimorph end displacement is obtained as Figure 16.

The amplitude of control voltage is 100 V, the frequency is 0.1 Hz. With the unclamped length is reduced by 2 mm (from 18.5 to 16.5 mm), the end displacement is reduced by 21.81 μm (from 106.63 to 84.82 μm). Based on model of deflector center displacement for limited feedback rod ball (equation (43)), the effect of bimorph unclamped length on deflector center displacement x_{dlim} while feedback rod ball is limited is obtained as Figure 17. With a control voltage of 100 V at 0.1 Hz, deflector center displacement is reduced by 20.80 μm (from 116.07 to 95.27 μm) while the unclamped length is reduced by 2 mm (from 18.5 to 16.5 mm).

Based on equations (10), (18), (24), and (42) obtained in section 3, while the control voltage amplitude is 100 V and the frequency is 0.1 Hz, single multilayer bimorph end displacement δ_1, the multilayer bimorph end displacement in the assembly for free feedback rod

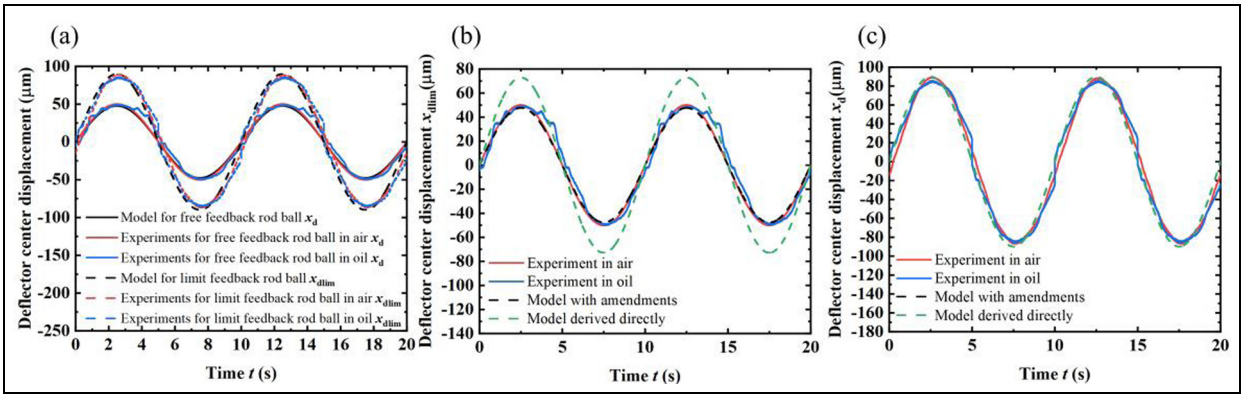

Figure 15. The comparison among results of: (a) model with amendments and experiments, (b) models and experiments while the feedback rod ball is limited, and (c) models and experiments while the feedback rod ball is free.

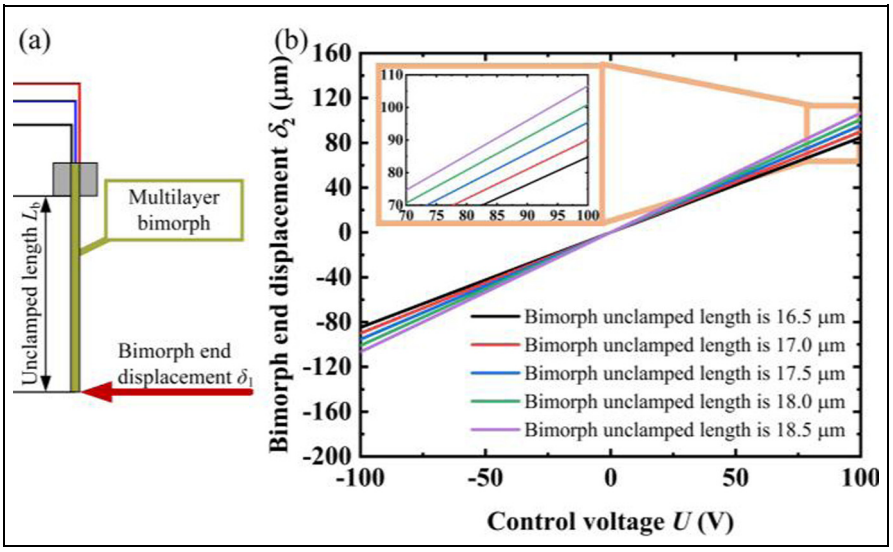

Figure 16. Effect of multilayer bimorph unclamped length on bimorph end displacement: (a) schematic diagram of monitoring variables, and (b) the multilayer bimorph end displacement.

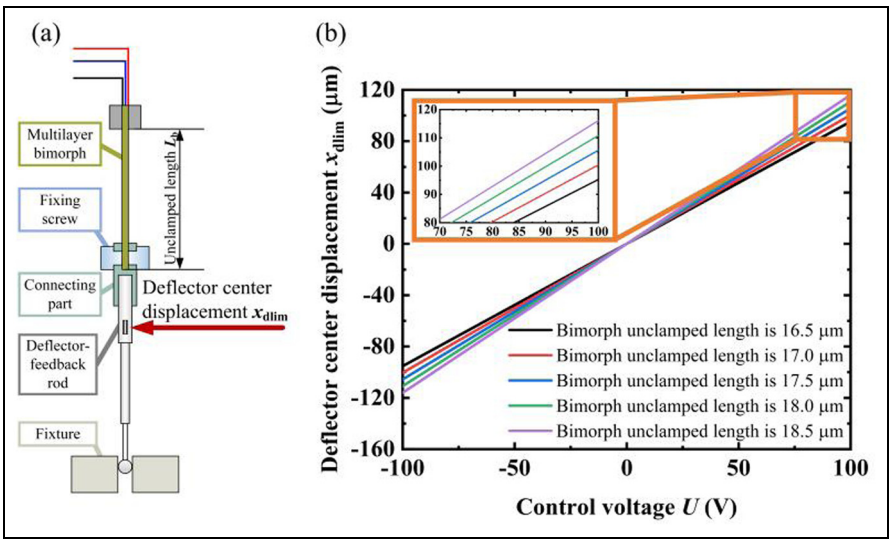

Figure 17. Effect of multilayer bimorph unclamped length on deflector center displacement while feedback rod ball is limited: (a) schematic diagram of monitoring variables, and (b) the deflector center displacement.

ball δ_2, the deflector center displacement in the assembly for free feedback rod ball x_d, and the deflector center displacement in the assembly for limited feedback rod ball x_{dlim} are compared in Figure 18.

The end displacement of a single multilayer bimorph is quite similar with the multilayer bimorph end displacement in the assembly for free feedback rod ball. The maximum deflector center displacement for free feedback rod ball reaches 179.71 μm, while the maximum deflector center displacement in the assembly for limited feedback rod ball only reaches 95.21 μm.

Based on the model of assembly end displacement for free feedback rod ball (equations (32) and (33)), the trajectory for free feedback rod ball is obtained as Figure 19.

While the amplitude of control voltage is 100 V and the frequency is 0.1 Hz, the axial feedback rod ball center displacement L_3 reaches 1.62 μm, and the feedback rod ball center displacement x_s reaches 371.57 μm.

The fitting clearance variation between the feedback rod ball and limit slot critically affects the assembly output linearity. When the clearance exists, the working status of the assembly is shown in Figure 20. While the feedback rod ball center displacement x_s which can be obtained by equation (32) does not reach the clearance, the feedback rod ball is considered to be free with the feedback force is 0, and the deflector center displacement x_{dc} can be obtained by equation (24). While the feedback rod ball center displacement x_s equals or exceeds the clearance, the feedback rod ball is

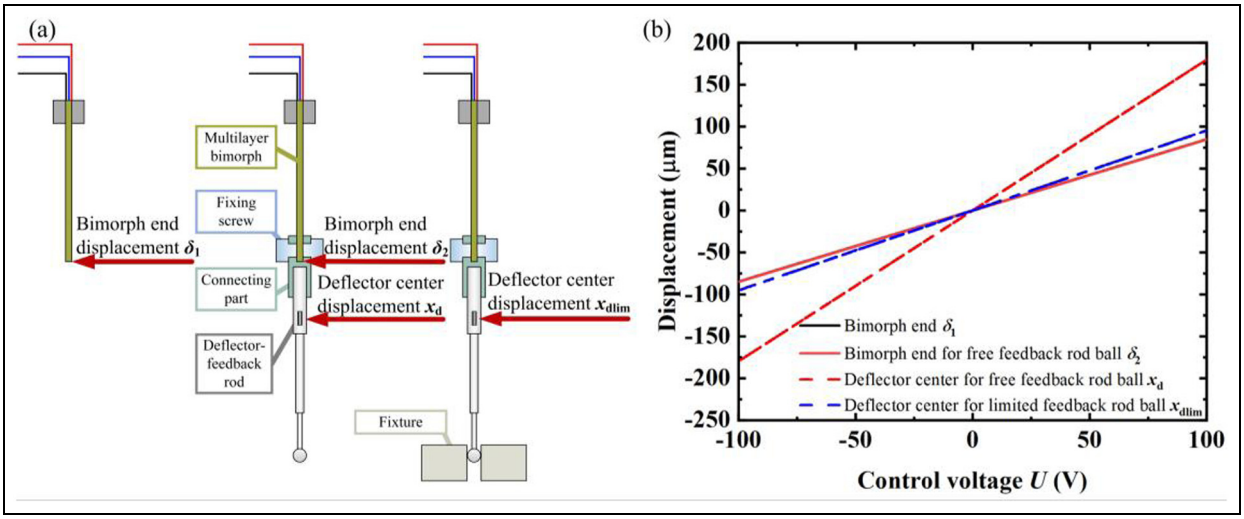

Figure 18. Bimorph end and deflector center displacement under different conditions: (a) schematic diagram of monitoring variables, and (b) displacement under different conditions.

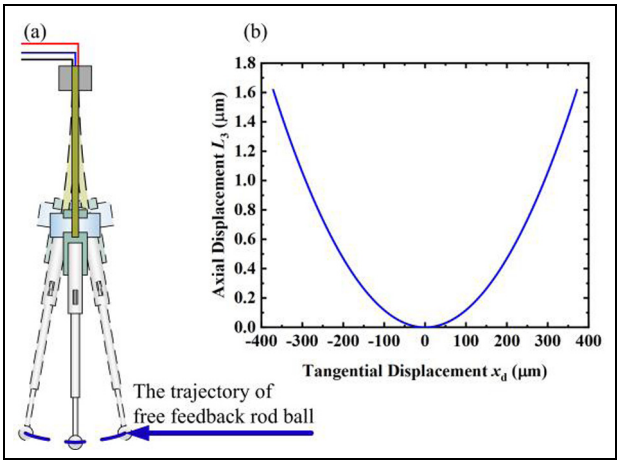

Figure 19. The trajectory of free feedback rod ball: (a) schematic diagram of monitoring variables, and (b) displacement under different conditions.

considered to be limited and the deflector center displacement x_{dc} can be obtained by equation (42).

Based on proposed model, the effect of different clearances on deflector center displacement and feedback force acted on the feedback rod ball are shown in Figure 21, while the amplitude of the control voltage is 100 V and the frequency is 0.1 Hz.

An abrupt change in feedback force and deflector center displacement occurs when the feedback rod ball contacts the fixture. Based on practical assembly conditions, the clearance between the feedback rod ball of the assembly and the limit slot can be controlled within 3 μm. When the clearance is 3 μm, the region for free feedback rod ball accounts for 0.97% of a cycle, and the magnitude of the displacement change suddenly when the feedback rod ball contacts the limit slot reaches 1.16 μm. Wider clearances result in longer operating durations under free feedback rod ball conditions, greater influence on output displacement. A smaller clearance is preferable to mitigate abrupt displacement variations and ensure control accuracy.

Conclusion

In this paper, based on the proposed structure, the mathematical model of multilayer bimorph and deflector-feedback rod assembly for deflection jet servo valves is established. The static characteristics of the multilayer bimorph and deflector-feedback rod assembly are conducted by simulation and experiments. The detailed conclusions are as follows:

(1) A new structure of the first stage assembly exposing the feedback rod is designed to meet the requirements that enable bimorph clamped length adjustment and relative positioning between bimorph and feedback rod adjustment. With the fixture, the characteristics of the assembly while the feedback rod ball is limited in oil can be tested.

(2) A mathematical model of the assembly that account for the anticlastic deformation is established under the actual working condition that the feedback rod ball is limited. Compared with experimental results, the maximum relative error of deflector center displacement in proposed model reaches 14.46%, while the maximum relative error of deflector displacement derived directly from traditional model reaches 80.46%.

(3) The effect of bimorph clamped length on feedback rod ball center displacement and the effect of feedback rod ball limitation on deflector center displacement can be obtained through

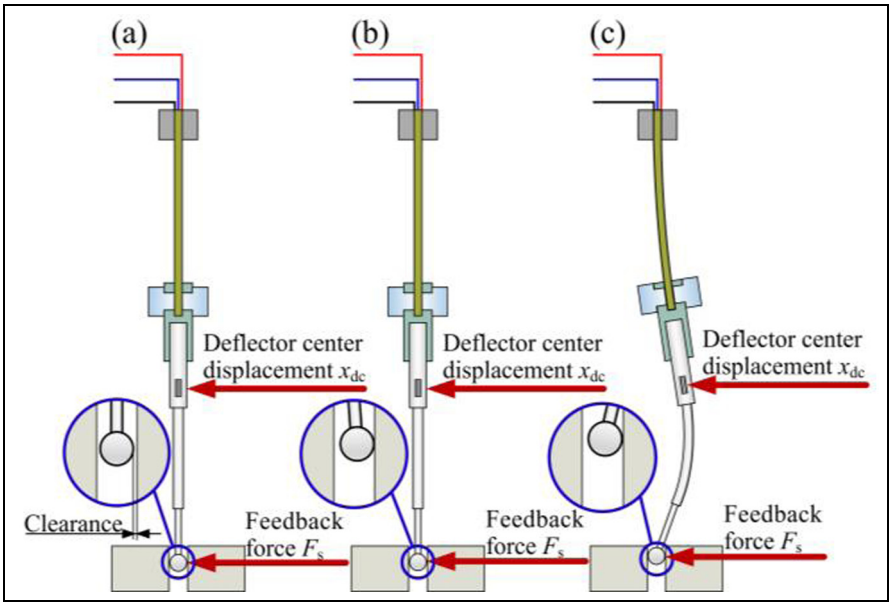

Figure 20. Assembly working states with clearance: (a) state when control voltage amplitude is zero, (b) initial contact state when feedback rod ball center displacement equals clearance, and (c) state when feedback rod ball center displacement exceeds clearance.

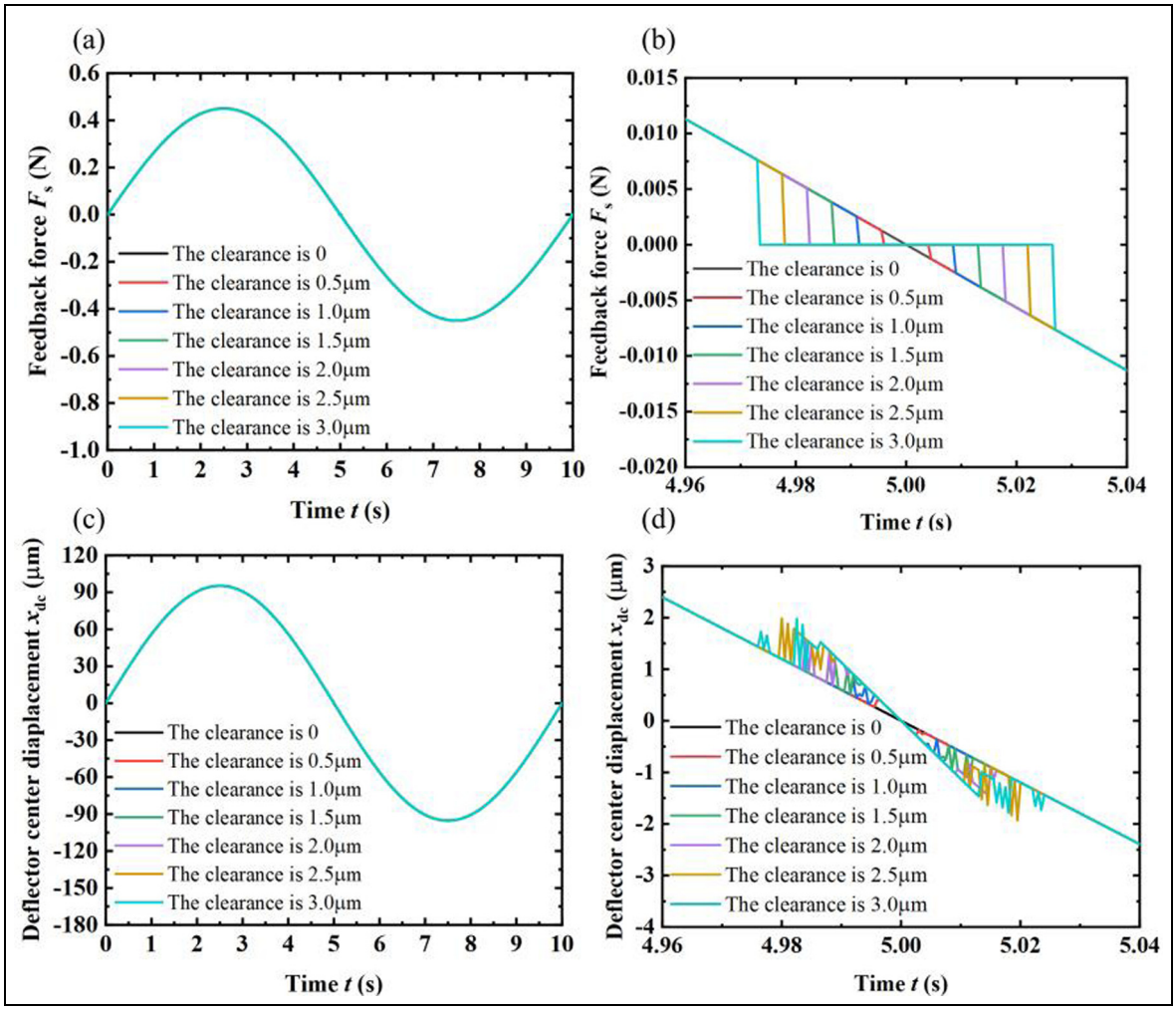

Figure 21. The effect of different clearance on output characteristics: (a) feedback force acted on feedback rod ball, (b) feedback force near zero control voltage, (c) deflector center displacement, and (d) deflector center displacement near zero control voltage.

mathematical model. While the amplitude of control voltage is 100 V and the frequency is 0.1 Hz, with the unclamped length is reduced by 10.81%, the deflector center displacement is reduced by 17.92%.

(4) Larger assembly end fitting clearance leads to longer operation period for free feedback rod ball movement, affecting continuity of deflector center displacement output. An abrupt change in feedback force and deflector center displacement occurs when the feedback rod ball contacts the fixture. With the clearance of 3 μm, the deflector center displacement changes reaching 1.16 μm in a sudden.

This study provides not only theoretical support and practical guidance for applying and designing the pilot stage used for deflection jet servo valves, but also theoretical support for multilayer bimorph applications in complex structural load.

ORCID iDs

Yunqi Li https://orcid.org/0009-0009-3454-3947
Yuchuan Zhu https://orcid.org/0000-0002-7399-1656

Funding

The authors disclosed receipt of the following financial support for the research, authorship, and/or publication of this article: This work is supported by National Natural Science Foundation of China (51975275), Aeronautical science foundation of China (No.20220007052001) and the International Joint Laboratory of Sustainable Manufacturing, Ministry of Education and the Fundamental Research Funds for the Central Universities (No.NG2024016).

Declaration of conflicting interests

The authors declared no potential conflicts of interest with respect to the research, authorship, and/or publication of this article.

References

1. Chen Z, Ge S, Jiang Y, et al. Mathematical modeling of pressure characteristics of the deflector-jet pilot stage considering boundary layer flow. *Flow Meas Instrum* 2023; 90: 102312.
2. Lv X, Yang J, Qi Q, et al. Mathematical modeling of an armature assembly in a flapper–nozzle servo valve based on the finite element method. *IEEE/ASME Trans Mechatron* 2024; 29: 3684–3695.
3. Karunanidhi S and Singaperumal M. Mathematical modelling and experimental characterization of a high dynamic servo valve integrated with piezoelectric actuator. *Proc Inst Mech Eng Part I-J Syst Control Eng* 2010; 224: 419–435.
4. Chen Z, Ge S, Jiang Y, et al. Refined modeling and experimental verification of a torque motor for an electro-hydraulic servo valve. *Chin J Aeronaut* 2023; 36: 302–317.
5. Al-Dweikat M, Zhang G, Liu Y, et al. A comparison of two piezoelectric actuator concepts for fast mechanical switching in dc hybrid circuit breakers. *Rev Sci Instrum* 2024; 95: 074709.
6. Ji HW, Lin LM, Liu Y, et al. Achieving smooth motion in displacement amplification piezoelectric stick-slip actuator. *Rev Sci Instrum* 2024; 95: 105002.
7. Xu Z, Liu T, Li X, et al. An impact inertial piezoelectric actuator with high thrust-weight ratio driven by coupling the inertial force and friction force. *IEEE Trans Ind Electron* 2024; 71: 16275–16285.
8. Qi J and Wang L. Development of a stick-slip piezoelectric actuator using bending deformation based on hammer-type driving foot. *Rev Sci Instrum* 2025; 96: 025004.
9. Zhang Y, Pan W, Chen S, et al. Mathematical modeling and experimental characterization of the piezoelectric servo valve system. *J Tribol Trans* 2024; 146: 014601.
10. Bertin M, Plummer A, Bowen C, et al. A dual lane piezoelectric ring bender actuated nozzle-flapper servo valve for aero engine fuel metering. *Smart Mater Struct* 2019; 28: 115015.
11. Tamburrano P, Sciatti F, Plummer AR, et al. A review of novel architectures of servo valves driven by piezoelectric actuators. *Energies* 2021; 14: 4858.
12. Plummer A. Electrohydraulic servo valves – past, present, and future. In: *Proceedings of the 10th international fluid power conference*, Dresden, Germany, 8–10 March, 2016.
13. Ling M and Wang J. Nonlinear coupled dynamic effects in flexure-amplified piezoelectric valve with an analytical transfer function. *Proc Inst Mech Eng C J Mech Eng Sci* 2023; 237: 359–373.
14. Han C, Choi SB and Han YM. A piezoelectric actuator-based direct-drive valve for fast motion control at high operating temperatures. *Appl Sci* 2018; 8: 1806.
15. Tamburrano P, De Palma P, Plummer AR, et al. Simulation of a high frequency on/off valve actuated by a piezo-ring stack for digital hydraulics. *E3S Web Conf* 2021; 312: 05008.
16. Tamburrano P, Plummer AR, De Palma P, et al. A novel servovalve pilot stage actuated by a piezo-electric ring bender: a numerical and experimental analysis. *Energies* 2020; 13: 671.
17. Sedziak D, Minorowicz B, Stefański F, et al. Modelling and investigations of piezobender used in control of electrohydraulic servo valve. In: *17th international Carpathian control conference (ICCC)*, 2016, pp.651-656.
18. Gui S, Zhang S, Fu B, et al. Fluid-dynamic analysis and multi-objective design optimization of piezoelectric servo valves. *Flow Meas Instrum* 2022; 85: 102157.
19. Banerjee A, Bera KK and Singha AK. Enhanced vibration control using non-reciprocal piezoelectric beam having sensing and actuating bimorph: spectral element formulation. *Compos Struct* 2024; 329: 117793.
20. Song J. *Research on design and characteristics of servo valve actuated by piezoelectric ceramics*. Master's Thesis, Harbin Institute of Technology, China, 2019.
21. Braun S, Haasl S, Sadoon S, et al. Small footprint knife gate microvalves for large flow control. In: *International*

conference on solid-state sensors, actuators and microsystems, 2005, pp. 329-332.
22. Cheng M, Wu J, Guan M, et al. A high-resolution electric field sensor based on piezoelectric bimorph composite. *Smart Mater Struct* 2022; 31: 025008.
23. Smits JG, Dalke SI and Cooney TK. The constituent equations of piezoelectric bimorphs. *Sens Actuator A-Phys* 1991; 28: 41–61.
24. Zhu L, E S, Zhu X, et al. Development of hydroelectric servo-valve based on piezoelectric elements. In: *2010 international conference on mechanic automation and control engineering*, 2010, pp. 3330-3333.
25. Milecki A and Rybarczyk D. Investigations of applications of smart materials and methods in fluid valves and drives. *J Mach Eng* 2019; 19: 122–134.
26. Chen X, Zhu Y, Gao Q, et al. Simulation research for fluid-solid interaction performance of a piezoelectric bimorph actuator applied in servo valves. In: *2019 IEEE 8th international conference on fluid power and mechatronics (FPM)*, 2019, pp.236–242.
27. Sangiah DK, Plummer AR, Bowen CR, et al. A novel piezohydraulic aerospace servo valve. Part 1: design and modelling. *Proc Inst Mech Eng I J Syst Control Eng* 2013; 227: 371–389.
28. Salmani H, Hanke U and Halvorsen E. Competing anticlastic and piezoelectric deformation at large deflections. *Smart Mater Struct* 2021; 30: 035019.
29. Ishihara D, Chigahalli Ramegowda P, Aikawa S, et al. Importance of three-dimensional piezoelectric coupling modeling in quantitative analysis of piezoelectric actuators. *Comput Model Eng Sci* 2023; 136: 1187–1206.
30. DeVoe DL and Pisano AP. Modeling and optimal design of piezoelectric cantilever microactuators. *J Microelectromech Syst* 1997; 6: 266–270.
31. Kioua H and Mirza S. Multilayer laminated piezoelectric bending actuators: design and manufacturing for optimum power density and efficiency. *Smart Mater Struct* 2000; 9: 476–484.
32. Zhang TT and Shi ZF. Bending behavior of 2–2 multilayered piezoelectric curved actuators. *Smart Mater Struct* 2007; 16: 634–641.
33. Skrzypacz P, Nurakhmetov D and Wei D. Generalized stiffness and effective mass coefficients for power-law Euler–Bernoulli beams. *Acta Mech Sin* 2020; 36: 160–175.
34. PZT Electronic Ceramic Co., Ltd. Data sheet: Piezo ceramic plate. PZT Piezo. https://www.pztpiezo.com/Content/upload/pdf/201914239/Piezo-ceramic-plate.pdf (2025, accessed November 5 2025)
35. CoreMorrow Ltd. Piezoelectric ceramic plate: key parameters and applications. Coremorrow. http://www.coremorrow.com/proshow-6-138-1.html (2018, accessed November 5 2025)
36. Zhang Z, Xia C, Qi G, et al. Multi-step state-based opacity for unambiguous weighted machines. *Sci China Inf Sci* 2024; 67: 212204.
37. Tian F, Yang C, Zhang E, et al. Design optimization of hydraulic machinery based on ISIGHT software: a review of methods and applications. *Water* 2023; 15: 2100.
38. Zhang Z, Xia C, Fu J, et al. Initial-state observability of mealy-based finite-state machine with nondeterministic output functions. *IEEE Trans Syst Man Cybern Syst* 2022; 52: 6396–6405.